Optimization of in-vivo murine X-ray dark-field computed tomography

Stephan Umkehrer,[1, a)] Lorenz Birnbacher,[1] Rico Burkhardt,[2, 3, 4] Maximilian von Teuffenbach,[1] Ali Önder Yildirim,[5] Daniela Pfeiffer,[6] Julia Herzen,[1] and Franz Pfeiffer[1, 6]

[1)] *Chair of Biomedical Physics, Physics Department & Munich School of BioEngineering, Technical University of Munich, Garching, Germany*

[2)] *Department of Radiation Oncology, Klinikum recht der Isar, Technical University of Munich, School of Medicine, Munich, Germany*

[3)] *Institute of Innovative Radiotherapy (iRT), Department of Radiation Sciences (DRS), Helmholtz Zentrum München, Neuherberg, Germany*

[4)] *Physics Department, Technical University of Munich, Garching, Germany*

[5)] *Comprehensive Pneumology Center, Institute of Lung Biology and Disease, Helmholtz Center Munich, Munich, Germany*

[6)] *Department of Diagnostic and Interventional Radiology, School of Medicine & Klinikum rechts der Isar, Technical University of Munich, Munich, Germany*

(Dated: 3 September 2019)

Grating-based dark-field interferometry can be realized with lab-based, low-brilliance X-ray sources and provides scattering information of sample structures below the detector pixel size. This unique property allows promising medical imaging applications, especially for lung diseases. Structural damage in lung tissue caused by pulmonary emphysema or pulmonary carcinoma could be observed in radiographs by changes in the dark-field signal with high sensitivity at early stages, in contrast to the conventional absorption signal.
Currently, the standard for diagnosis in the clinical routine of pulmonary diseases is absorption CT. The assessment of a larger number of samples with in-vivo dark-field CT is limited by the rather long scan times, the order of 2 hours, that are required to obtain sufficient CT data quality. In this work, a prototype in-vivo, small-animal, dark-field CT is optimized with respect to CT measurements with the following: usage of an iterative reconstruction algorithm for the reduction of undersampling artifacts, a rearranged data acquisition scheme with reduced amount of dead time, and thinned gratings and curved grating geometry for more efficient utilization of the 37 kV X-ray flux. The device performance is evaluated with noise-effective dose measurements, image contrast-to-noise ratio, interferometry visibility across the field-of-view, and a reduced measurement time of 40 minutes with a deposited dose of 85 mGy.

PACS numbers: Valid PACS appear here
Keywords: Dark-field imaging, Dark-field computed tomography

I. INTRODUCTION

Grating-based phase-contrast and dark-field imaging is an X-ray interferometry-based technique, which provides additional contrast information in comparison with to the conventional absorption-based radiography[1,2]. Originally developed at synchrotron facilities, grating-based dark-field and phase-contrast interferometry can also be realized using low-brilliance lab-based X-ray sources enabling a wide use especially in medical applications[3–5]. This method implies the use of a three-grating Talbot-Lau interferometer, which is placed in the beam, providing three complementary image signals: attenuation, phase-contrast, and dark-field. In the attenuation image, which visualizes highly absorbing tissue such as bone structures, the depiction of different soft-tissue types such as muscle or fat tissue is very difficult due merely minor differences in the respective densities. In comparison, the phase-contrast image is based on refraction in the sample and provides high soft-tissue contrast. The dark-field signal reveals small-angle scattering information of, for example, microcalcifications or of multiple interfaces with strongly differing refractive indices[6,7].
An X-ray phase-contrast and dark-field CT scanner for small animals has been developed over the past few years[8,9]. The dark-field signal is highly sensitive to scattering by the alveoli in the lung[10], therefore first experimental results with this scanner could successfully demonstrated the potential of dark-field radiography for detection and staging of pulmonary diseases such as pulmonary emphysema[11–13], pulmonary fibrosis[14], and pulmonary carcinoma[15–17]. Healthy alveolar lung tissue causes a strong dark-field signal, as multiple scattering between air and the alveolar tissue occurs. Structural pathological changes in the lung tissue due to reduction of the number of alveoli can then be observed by a decreased dark-field signal[6,7].
The feasibility of computed tomography (CT) with this setup could be shown by Tapfer et. al.[9]. First promising results of in-vivo dark-field CT of pulmonary emphysematous and fibrotic mice have been published by Velroyen et al.[18]. In-vivo imaging implies the need to anaesthetize the animals, which is medically limited. Moreover, the scan time for one CT measurement was rather long, and the reconstructed volumes suffered from too many artifacts for a reliable diagnosis.

[a)] Electronic mail: stephan.umkehrer@ph.tum.de

In this work, we indicate how to reduce the total measurement duration of this small animal grating-based phase-contrast and dark-field CT scanner without loss of image quality. In detail, we analyzed the noise equivalent dose (NED) and optimized the data acquisition protocol. Additionally, we implemented a new grating configuration by bending the phase and analyzer gratings dependent on their respective radius from the source to increase flux and visibility, since plane grating geometry suffers from shadowing artifacts[19,20]. With our optimization we could significantly reduce the exposure time and consequently the accumulated dose for in-vivo small animal dark-field CT.

II. MATERIALS AND METHODS

A. Experimental Setup

The small animal X-ray dark-field CT setup presented in our work was developed in collaboration with Bruker MicroCT (formerly Skyscan)[8,9]. The grating-interferometer was adapted to fit into the housing of a typical micro-CT. The dark-field and phase-contrast small-animal scanner consists of a rotating gantry system enabling tomographic scans with a stationary sample thus allowing in-vivo measurements. The compact micro-CT has different equipment for monitoring physiological functions such as breathing, heart beat, and body temperature. The gantry system features a direct anode tungsten target X-ray tube (RTW, MCBM 65B-50 W) with a focal spot size of $50 \times 50\,\mu m^2$, a Hamamatsu flat panel detector (C9312SK-06) with a gadolinium oxysulfide (GOS) scintillator, a pixel size of $50 \times 50\,\mu m^2$, and an active area of 2472×2184 pixel, as well as a Talbot-Lau interferometer working in the first fractional Talbot order. The interferometer consists of a source grating G_0 (period 10 µm; gold filling height 35 µm), a phase grating G_1 (period 3.24 µm; nickel height 4 µm; $\pi/2$ phase-shift), and an analyzer grating G_2 (period 4.8 µm; gold filling height 45 µm). The design energy of the system is 23 keV. A photograph of the setup and a technical drawing of the interferometer can be seen in Figure 1. The thickness of the silicon wafer for G_1 is $d_{\mathsf{wafer},1} = 550\,\mu m$, whereas the substrate thickness of G_0 and G_2 are $d_{\mathsf{wafer},0/2} = 200\,\mu m$ each. All gratings are deposited on silicon substrates and were fabricated according to the LIGA (German acronym for **Li**thographie, **G**alvanoformung, **A**bformung) process[21–24]. The source-to-sample and sample-to-detector distances are 250 mm and 200 mm, respectively. Due to magnification, the effective pixel size in the sample plane is $29 \times 29\,\mu m^2$. More details of the development of the scanner can be found in Tapfer et al.[8,9].

B. Radiation Dose Evaluation

As some of the measurements presented in this work were performed in-vivo, it was necessary to estimate the radiation exposure dose per second. Therefore, a patient skin dosimeter (Unfors PSD, Unfors Instruments AB, Billdal, Sweden) was placed in the center of a polymer cylinder with a diameter of 3 cm. The polymer material is similar in density to carbon and is a good approximation of a mouse phantom[25]. To avoid statistical errors, the dosimeter was placed in the beam for 10 minutes, and the radiation dose rate (Gy/s) was averaged from the measured value.

C. Phantom

A water filled 3D printed tube is used as a dark-field phantom. It consists of earplugs wrapped in plastic foil simulating the lung. Two additional features are inserted into the tube: One rod of polyvinylchloride (PVC), which is highly absorptive and simulates the bones, and one rod of polymethylmethacrylate (PMMA) which mimics phase-contrast information and simulates the absorption of soft tissue.

D. Murine Model

Animal experiments were performed with permission of the Institutional Animal Care and Use Committee of the Helmholtz Center Munich and carried out in accordance with national (Gesellschaft für Versuchstierkunde - Society for Laboratory Animal Science) and international (Federation for Laboratory Animal Science Associations) animal welfare guidelines. The Institutional Animal Care and Use Committee of the Helmholtz Center Munich approved all the experimental protocols under the numbers 2532-77-12 and project number 55.2-1-54-2532.120.2015, respectively. For the experiments, mice were anesthetized using intraperitoneal injection of medetomidine (500 µg/kg), midazolam (5 mg/kg), and fentanyl (50 µg/kg). The mice were placed onto the sample bed inside the scanner in a dorsal position. During the measurements the mice breathed freely, and body temperature as well as the respiratory frequency were monitored. A fan inside the scanning chamber protected the mice against hyperthermia. The experiments were carried out within the framework of other animal studies and not expressly to emphasize the optimization of the setup. The presentation here serves exclusively to illustrate and compare the two acquisition protocols. In-vivo measurements are presented to illustrate the influence of breathing and heart beat during image acquisition, which cannot be realized using ex-vivo or phantom measurements.

E. Data Acquisition

To process and obtain the images with the different contrast modalities a phase-stepping routine of the source grating was performed[2]. If not stated otherwise, the CT data set was acquired by executing $N = 211$ angular projections with each $n = 4$ grating steps and an exposure

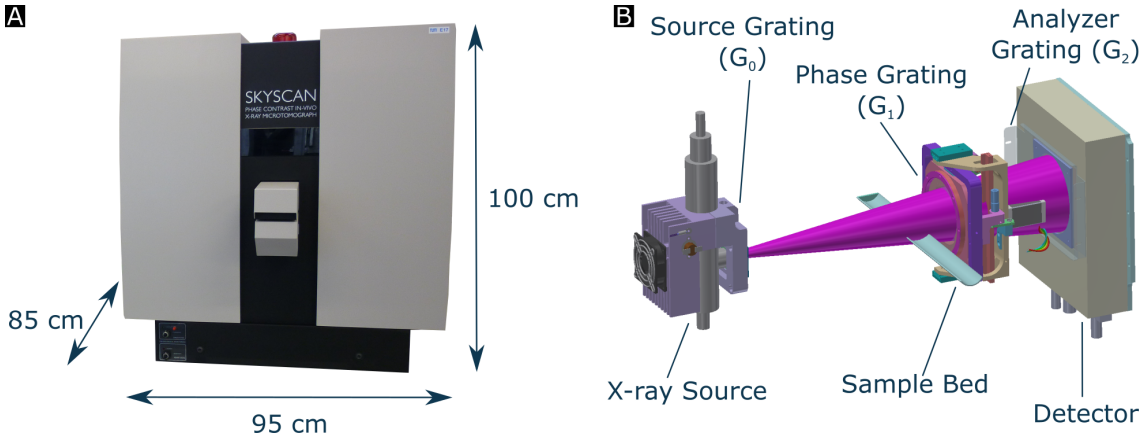

FIG. 1. *Photograph and sketch of the small-animal X-ray phase-contrast and dark-field CT scanner. (A) shows a photograph of the compact micro-CT housing with its dimensions. (B) depicts a technical drawing of the rotating gantry with the Talbot-Lau interferometer.*

time of $t_{\mathsf{exp}} = 1.43\,\mathrm{s}$, resulting in a total measurement time of $T_{\mathsf{Total}} \approx 40\,\mathrm{min}$. The detector was operated in 2×2 binning mode, resulting in an effective pixel size of $58 \times 58\,\mu\mathrm{m}^2$. The voltage was set to 37 kVp, the current was 661 µA resulting in 24 W source power. The accumulated dose was approximately 85 mGy, which is comparable with the dose delivered to a mouse in a conventional micro-CT system[25]. To use the total exposure time most efficiently, the sample scan was performed separately from the reference scan with both having the same parameters.

F. Processing and Reconstruction

The data handling was performed using internal python scripts. An expectation-maximization EM algorithm was used[26,27] to extract the phase-stepping signals. This algorithm compensates mechanical and thermal fluctuations in the measured intensity curve via a log-likelihood function.
For the three dimensional reconstruction of the processed data, we used a more advanced reconstruction algorithm, namely statistical iterative reconstruction (SIR)[28], that is able to reduce undersampling artifacts of sparsely acquired data[29]. In contrast to the widely used filtered backprojection (FBP), the Nyquist criterion necessary for sufficient data sampling, $N_\theta = N_{ray}\frac{\pi}{2}$[30,31], does not have to be fulfilled. N_θ is the number of angular projections distributed over 360°and N_{ray} is the number of sampling points in horizontal the direction in each projection.

G. Noise Equivalent Dose

The noise equivalent dose (NED) is a metric to compare and quantify the low-dose image quality of detectors[32]. With the help of the NED, the shortest reasonable exposure time can be estimated. The NED reveals the dose of incoming X-rays at which the X-ray photon shot noise signal sensitivity (NED_{PH}) is equal to the electrical noise level (NED_{DET}) of the detector system[32], i.e. the lower the NED value, the better the image quality under low-dose conditions. Without the presence of X-rays, the detector output signal is the detector readout noise and dark-current. In contrast, when an X-ray signal is produced and detected, the relative influence of the detector noise is reduced and can be ignored for strong signals.

III. RESULTS

The available measurement time for in-vivo experiments is limited due to anesthesia. To obtain images of the highest achievable quality for this limited time, data acquisition must be as efficient as possible. First, we optimized the data acquisition protocol to increase the image quality of the reconstructed volume. Second, the grating configuration and geometry were improved to increase the flux and visibility at the borders of the grating substrate.

A. Data Acquisition

As a first step towards reducing the data acquisition time, the lower exposure time limit was determined by analyzing the noise equivalent dose (NED). Measurements with 15 different exposure times between $t_{\mathsf{exp}} = 0.12\,\mathrm{s}$ and $t_{\mathsf{exp}} = 3.33\,\mathrm{s}$ were performed. For each exposure time, 60 phase-stepping measurements were carried out. The images were processed and the mean pixel value and the variance were extracted in different regions of interests (ROIs). With the gratings in the beam, the NED for the conventional attenuation signal is reached after 0.17 s of exposure.
In general, movement of the gratings or rotation of the gantry take up a large share of the measurement time, which needs to be reduced to increase the efficiency of use of the total measurement time. The phase-stepping routine requires at least three grating positions for the

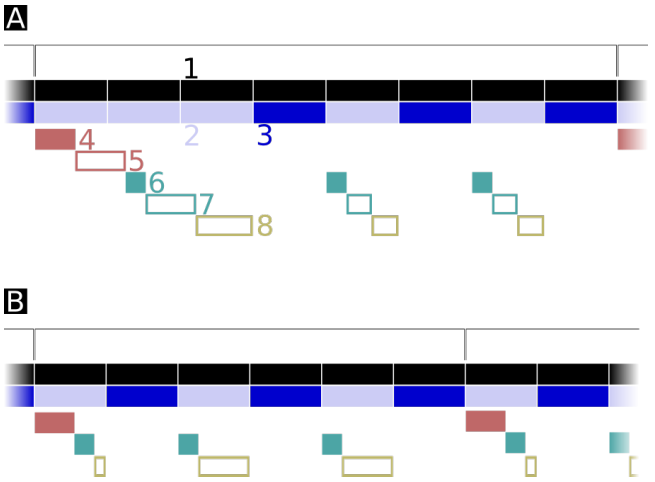

FIG. 2. *Scheme of the readout procedure of the setup. (A) shows the read-out of the detector with delay parameters and (B) shows the readout of the detector without delays. 1. Detector integration period, 2. Skipped image acquisition, 3. Used image acquisition, 4. Gantry rotation, 5. Gantry delay, 6. Grating movement, 7. Grating delay, 8. Waiting time till next frame.*

processing. However, measurements with three grating steps are prone to artifacts, for which reason we executed measurements at the lower limit for stable performance using $n = 4$ grating steps. To ensure satisfactory image quality and reduce undersampling artifacts for the SIR algorithm, a sufficient number of angular projections is needed. Using filtered backprojection and applying the Nyquist criterion, one would need at least 943 angular projections for a field of view of approximately 600 pixels in horizontal direction. However, using the SIR algorithm, we could empirically reduce the number to 211 projections with still sufficient quality.

The detector reads out in a continuous image acquisition mode in fixed image frames. A scheme of the detector readout behavior for one angular projection with and without delay parameters can be seen in Figure 2 A and B, respectively. By way of example, the image acquisition is depicted with three grating steps. The length of one image frame is defined by the exposure time. The delay parameters were implemented in previous software versions to add a pause after any movement and consequently to avoid the detection of the signal with vibrating gratings and thus image artifacts. Due to a software update and the implementation of an automatically skipped first image frame, where all the movement take place, the delays have in the meantime become unnecessary. Every image frame, which is affected by any movement of gantry or grating, or is influenced by a delay time is skipped. As additional delay parameters in the data acquisition result in further skipped image frames, and therefore increases the rate of loss time, the delay parameters are set to zero.

Based on the value of the NED and the detector readout, the exposure time for a single image is shortened from 5.00 s to 1.43 s for each image of the stepping routine, which is still more than eight times the noise equivalent integration time. The exposure time of 1.43 s is long enough to skip just one image frame for each angular projection and grating step. In addition, it is sufficient to avoid vibrations of the gratings during data acquisition, which result in a smeared fringe pattern of the stepping curve. The time gained by this reduction is used for additional angular projections to reduce the amount of undersampling artifacts. Furthermore, the voltage is increased from 35 kVp to 37 kVp to increase the flux. All acquisition parameters are given in Table I.

	Old	**New**
Exposure time [s]	5.00	1.43
Projections N [#]	139	211
Grating steps n[#]	5	4
Voltage [kV]	35	37
Current [µA]	592	661
Total scan time [min]	115	40

TABLE I. Acquisition parameters of the old[18] and the new data acquisition protocol.

A comparison of representative CT reconstruction slices of in-vivo mice measurements for conventional transmission and dark-field signal of the old[18] and the new developed acquisition protocol can be seen in Figure 3. The initial acquisition protocol is labeled **Old** in Table I and is represented by Figure 3 A, C, E, G. The new acquisition protocol is labeled **New** in Table I and shown in Figure 3 B, D, F, H. The new data acquisition protocol leads to a significant reduction in undersampling artifacts in the conventional attenuation signal (see Figure 3 A-D) even though the total exposure time and therefore the radiation dose is decreased. Compared to the old acquisition protocol, the sample borders are sharpened and the volume appears more homogeneous, so that small features are clearly visible and detectable. The image quality is also improved for the coronal slices. The grainy and noisy pattern is considerably reduced using the new acquisition protocol. Likewise, the improvements are distinctly recognizable in the dark-field signal (see Figure 3 E-H). Compared to the old acquisition protocol, small structures of the lung with the airways appear in the axial slices and coronal slices, respectively. The dark-field signal of the lung is more homogeneous and borders are sharpened.

In general, the image quality has been improved, whereas the total exposure time is decreased. The accumulated dose deposited in the mouse has been reduced from 200 mGy to 85 mGy, which is comparable with the dose delivered to a mouse chest in a conventional micro CT[25].

B. Grating Optimization

With a plane grating configuration, the X-rays do only impinge perpendicular to the optical axis. The angle of incidence α depends on the distance x between the grating structures and the optical axis and the source-to-grating distance L and can be expressed as $\alpha = \arctan(x/L)$. As a consequence, X-rays impinging offside the optical axis see a flattened intensity profile leading to a decreased intensity and a drop in visibility.

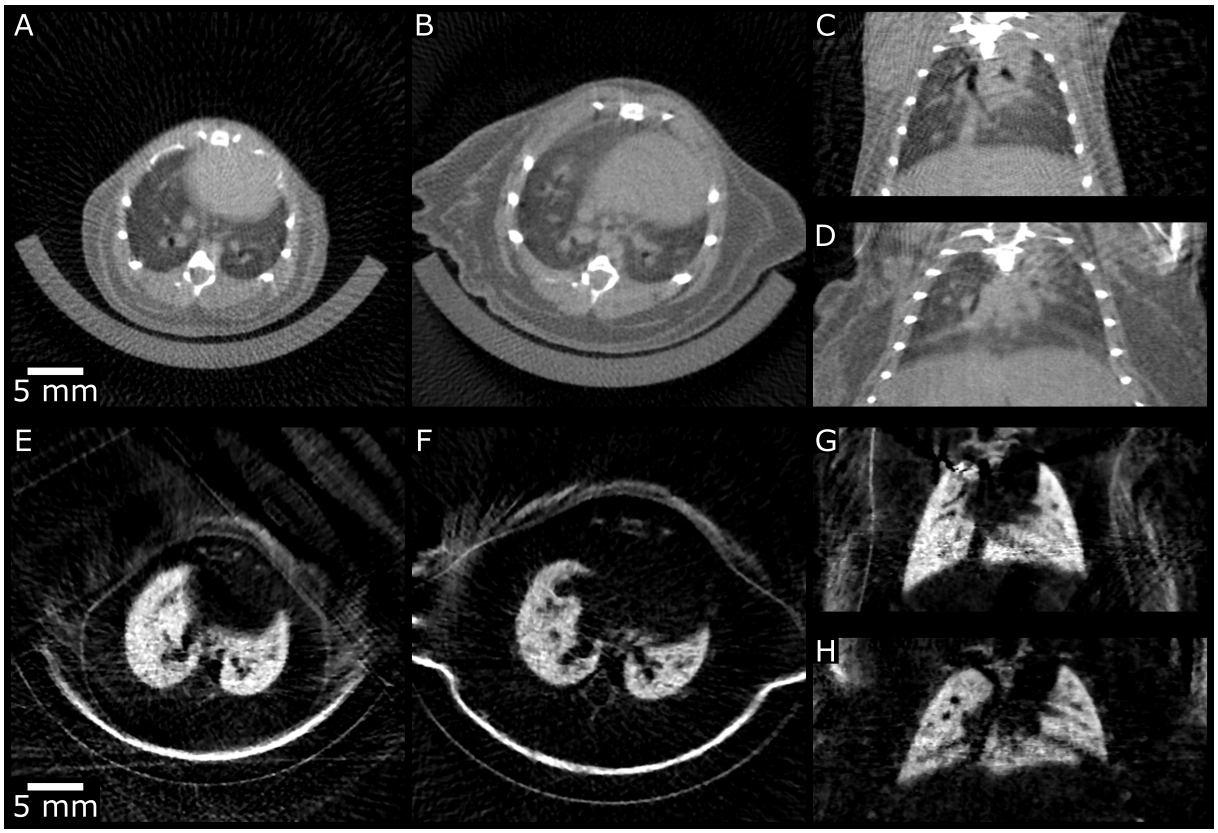

FIG. 3. *Comparison of two tomographic scans with the old and new data acquisition scheme. Transmission (top) and dark-field (bottom) CT slices of two in-vivo mice are presented. The images are scaled consistently within the same modality. The detector was operated in a* 2×2 *binning mode. The old image acquisition (A, C, E, G) can be compared with the new acquisition protocol (B, D, F, H). Typical axial (A, B) and coronal slices (C, D) of attenuation CT are shown. Representative slices of dark-field CT in (E, F) and coronal direction (G, H) are presented. The attenuation reconstruction as well as dark-field reconstruction show significant improvements in image quality with the new acquisition protocol. The impact of undersampling artifacts is clearly reduced by the new acquisition protocol, while the accumulated dose is decreased.*

Forcing the gratings on a radius corresponding to the distance to the source compensates for this effect and shifts the angle of incidence constantly to zero over the full field of view. The two different types of mountings for phase-grating and analyzer grating were adapted so that the curvature of the phase-grating G_1 corresponds to a radius of 30 cm, whereas the radius of the analyzer grating G_2 is 45 cm. In addition, the grating substrate of the old phase-grating G_1 with a thickness of 500 µm is replaced by a new phase-grating G_1 on a thinner substrate of 200 µm. The new grating G_1 features a period of 3.24 µm and a gold height of 2.30 µm, and also induces a phase-shift of $\pi/2$ as presented in Section II A.

To evaluate the performance of the curved grating configuration compared to the plane gratings, an image acquisition procedure with four phase steps was performed by stepping the source grating G_0 over one period perpendicular to the grating structures. The intensity can be extracted as the mean value of the phase-stepping curve, which can be approximated by a sine curve, whereas the visibility is defined as the amplitude of the phase-stepping curve divided by the mean. Measurements were performed without any object in the beam. In Figure 4, the results of the intensity (A) and the visibility (B) can be seen as a function of the pixel column. The orange lines represent the measurements performed with the thicker G_1 substrate, and plane G_1 and G_2. Measurements represented by the blue lines were conducted with the thinner G_1 substrate, and curved G_1 and G_2. The solid lines indicate the average over the pixel columns perpendicular to the grating lines, while the dashed lines represent the mean value over the whole image region. The results are summarized in Table II. For the plane gratings, both the intensity and the visibility drops strongly as the distance to the optical axis increases. The intensity and the visibility at the edges drops to 41% of the maximum intensity. In contrast the curved gratings, the value for intensity and visibility remain close to the value at the optical axis. Even at the minimum position, the visibility remains at 93% of the maximum value, while the intensity drops to just 77%. The remaining drop of the intensity and slight variation of the visibility can mainly be explained by the source grating G_0. The source-to-grating distance of G_0 is just 3 cm, so the grating would need a very small bending radius which implies a high risk of breaking the grating. Therefore, a plane grating is retained here. However, it contributes to the shadowing and the drop of visibility by flattening the perfect rectangular profile. Additionally, the thinner substrate of the phase-grating results in

	Plane	Bent
$\bar{I}_0 \times 10^4$ [a.u.]	4.13	5.94
$I_{0,\mathrm{min}} \times 10^4$ [a.u.]	2.39	5.05
$I_{0,\mathrm{max}} \times 10^4$ [a.u.]	5.82	6.53
$I_{0,\mathrm{min}}/I_{0,\mathrm{max}}$	0.41	0.77
$\bar{V}$ [%]	27.9	31.7
V_{min} [%]	13.3	30.3
V_{max} [%]	32.5	32.6
$V_{\mathrm{min}}/V_{\mathrm{max}}$	0.41	0.93

TABLE II. Results of the measurements performed with the two different grating configurations. Images were acquired using an exposure time of 1.43 s.

Material	Configuration	CNR_{ATT}	CNR_{DFI}
Earplug	plane	9.40	4.69
	bent	14.12	6.72
PMMA	plane	23.66	1.22
	bent	55.98	0.65
PVC	plane	48.49	2.25
	bent	79.33	3.10
Water	plane	28.91	0.92
	bent	60.60	0.72

TABLE III. Results of the CNR analysis, which was performed with the two different grating configurations but same data acquisition protocol.

an increased flux.
Measurements with the 3D printed phantom introduced in Section II C were performed with plane and curved grating configurations to investigate the CT performance of the optimization with curved gratings. The CT data were recorded using the new acquisition protocol as presented in Table I and the data was analyzed with a contrast-to-noise (CNR) measurement for different ROIs and materials. Slices of the reconstructed volume of bent and plane grating configurations can be seen in Figure 5. The squared regions in the individual features (PVC rod, PMMA rod, water, earplug) in the axial slices were selected and can be seen in Figure 5. To improve statistics, the mean and standard deviation were analyzed over the average of 100 adjacent slices. The CNRs were calculated between the respective feature and background regions using the conventional attenuation signal (ATT) as well as in dark-field images (DFI). The results of the CNR analysis are listed in Table III. The presented CNR values demonstrate clearly that the new grating configuration with the bent gratings is an improvement over the plane gratings. This can be explained by the increased total flux and therefore a reduced effect of the constant readout noise especially at the edges of the angular projections and a homogeneous visibility over the whole ROI.

IV. CONCLUSION

In this work, we report on an optimization of the image quality of the first dark-field small animal CT scanner. Both the attenuation and dark-field data of in-vivo mice improved significantly. In-vivo measurements are presented in order to illustrate the influence of movements of the specimen during acquisition, which cannot be realized for ex-vivo or phantom measurements. The in-vivo measurements were not conducted just to present the improvements of the acquisition protocol, rather they were executed within different animal studies. Firstly, the data acquisition procedure of the scanner was analyzed. The effect of the exposure time and the number of grating steps per angular projection image was investigated with respect to the total measurement time. A new image acquisition protocol was developed. Compared to the prior acquisition protocol used in a proof-of-principal study, the number of angular projections could be increased by more than 50% although the total exposure time is reduced from approximately two hours to 40 min.[18] In addition, the accumulated dose is significantly reduced from from 200 mGy to 85 mGy.
In addition, hardware optimization was achieved. A plane grating geometry leads to a drop of visibility and

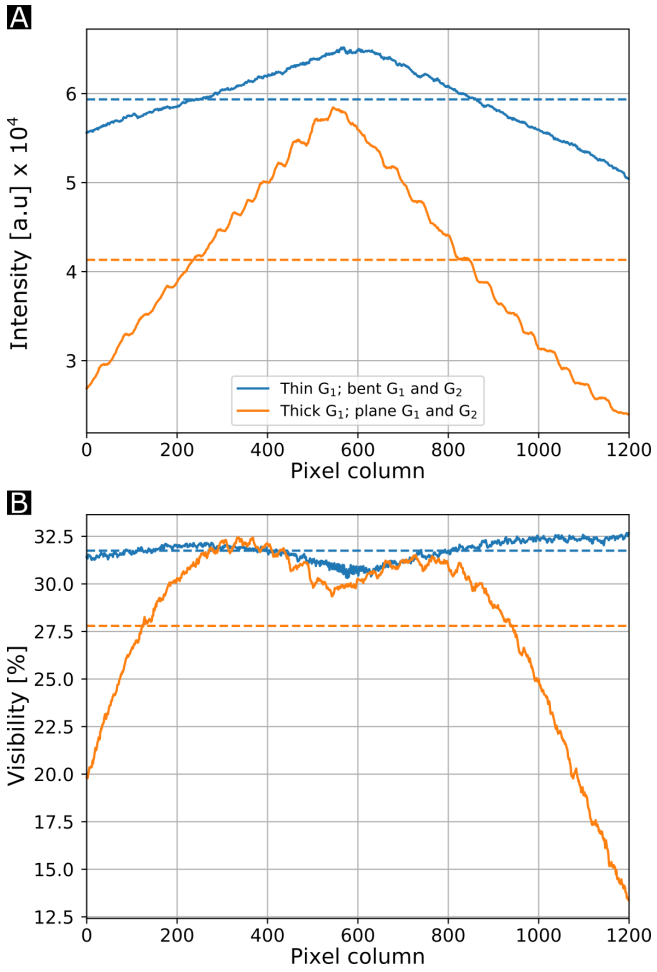

FIG. 4. *Comparison of curved and plane grating configuration. (A) shows the mean intensity measured at the detector pixel columns. (B) shows the visibility of the stepping curve as a function the pixel column. The solid lines indicate the value per column, the dashed lines represent the mean value over the whole ROI. The lines in blue represent the new and curved gratings, and the old plane gratings are represented in orange. The drop of intensity and visibility at the edges is clearly reduced by bending the phase and analyzer gratings.*

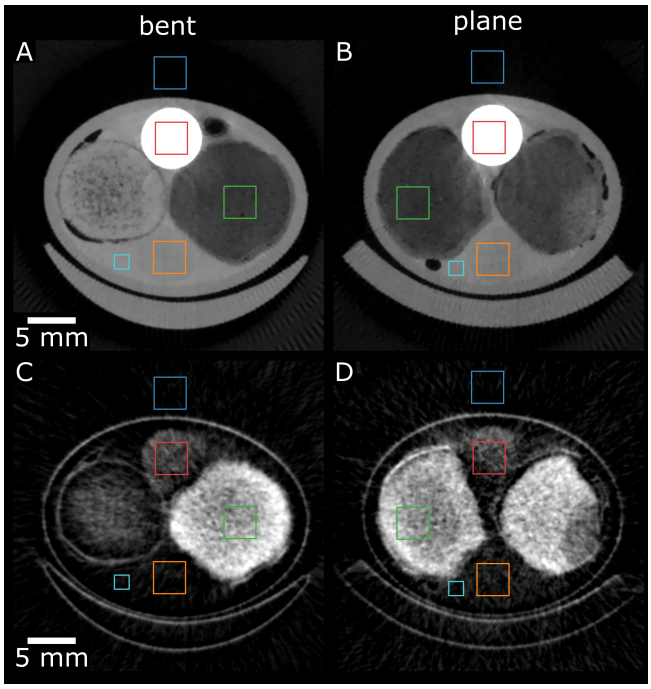

FIG. 5. *Phantom measurements using curved grating configuration (A, C) and plane grating configuration (B, D). The images are scaled consistently within the same modality. Regions of interest for the CNR analysis are indicated by the colored rectangles: PMMA rod (orange), earplug (green), PVC rod (red), water (cyan), and the background intensity (blue). The images were acquired using the same data acquisition protocol.*

intensity of pixels offside the optical axis. Therefore, the phase-grating and the analyzer grating G_2 were bent with a radius of curvature corresponding to their respective distance to the source. This curved grating geometry results in a perpendicular angle of incidence of the X-rays to the gratings over the whole field of view. As a consequence, this avoids the drop of visibility and intensity especially at the sample border leading to additional improvements in the image quality. Furthermore, we installed a new phase-grating G_1 on a thinner substrate, resulting in additional flux over the whole image.
The improvements of the data acquisition protocol with the decreased accumulated dose and total exposure time will permit future investigations on different pulmonary diseases. Studies of in-vivo mice with different pulmonary diseases using a statistically relevant number of specimens can now be performed more easily. This can be seen as an essential first step towards the evaluation of in-vivo dark-field CT measurements.

V. ACKNOWLEDGMENTS

We acknowledge financial support through the European Research Council (ERC, H2020, AdG 695045), the DFG Cluster of Excellence Munich-Centre for Advanced Photonics (MAP, EXC158), and the DFG Gottfried Wilhelm Leibniz program. This work was carried out with the support of the Karlsruhe Nano Micro Facility (KNMF, www.kit.edu/knmf), a Helmholtz Research Infrastructure at Karlsruhe Institute of Technology (KIT).

REFERENCES

[1] C. David, B. Nöhammer, H. H. Solak, and E. Ziegler, Applied Physics Letters **81**, 3287 (2002).
[2] T. Weitkamp, A. Diaz, C. David, F. Pfeiffer, M. Stampanoni, P. Cloetens, and E. Ziegler, Optics Express **13**, 6296 (2005).
[3] F. Pfeiffer, T. Weitkamp, O. Bunk, and C. David, Nature Physics **2**, 258 (2006).
[4] F. Pfeiffer, M. Bech, O. Bunk, P. Kraft, E. F. Eikenberry, C. Brönnimann, C. Grünzweig, and C. David, Nature Materials **7**, 134 (2008).
[5] F. Pfeiffer, C. Kottler, O. Bunk, and C. David, Physical Review Letters **98**, 108105 (2007).
[6] S. Schleede, F. G. Meinel, M. Bech, J. Herzen, K. Achterhold, G. Potdevin, A. Malecki, S. Adam-Neumair, S. F. Thieme, F. Bamberg, *et al.*, Proceedings of the National Academy of Sciences **109**, 17880 (2012).
[7] K. Scherer, E. Braig, S. Ehn, J. Schock, J. Wolf, L. Birnbacher, M. Chabior, J. Herzen, D. Mayr, S. Grandl, *et al.*, Scientific Reports **6**, 36991 (2016).
[8] A. Tapfer, M. Bech, B. Pauwels, X. Liu, P. Bruyndonckx, A. Sasov, J. Kenntner, J. Mohr, M. Walter, J. Schulz, *et al.*, Medical Physics **38**, 5910 (2011).
[9] A. Tapfer, M. Bech, A. Velroyen, J. Meiser, J. Mohr, M. Walter, J. Schulz, B. Pauwels, P. Bruyndonckx, X. Liu, *et al.*, Proceedings of the National Academy of Sciences **109**, 15691 (2012).
[10] M. Bech, A. Tapfer, A. Velroyen, A. Yaroshenko, B. Pauwels, J. Hostens, P. Bruyndonckx, A. Sasov, and F. Pfeiffer, Scientific Reports **3**, 3209 (2013).
[11] A. Yaroshenko, F. G. Meinel, M. Bech, A. Tapfer, A. Velroyen, S. Schleede, S. Auweter, A. Bohla, A. Ö. Yildirim, K. Nikolaou, *et al.*, Radiology **269**, 427 (2013).
[12] F. G. Meinel, A. Yaroshenko, K. Hellbach, M. Bech, M. Müller, A. Velroyen, F. Bamberg, O. Eickelberg, K. Nikolaou, M. F. Reiser, *et al.*, Investigative Radiology **49**, 653 (2014).
[13] K. Hellbach, A. Yaroshenko, F. G. Meinel, A. Ö. Yildirim, T. M. Conlon, M. Bech, M. Müller, A. Velroyen, M. Notohamiprodjo, F. Bamberg, *et al.*, Investigative Radiology **50**, 430 (2015).
[14] K. Hellbach, A. Yaroshenko, K. Willer, T. M. Conlon, M. B. Braunagel, S. Auweter, A. Ö. Yildirim, O. Eickelberg, F. Pfeiffer, M. F. Reiser, *et al.*, Scientific Reports **7**, 340 (2017).
[15] F. G. Meinel, F. Schwab, A. Yaroshenko, A. Velroyen, M. Bech, K. Hellbach, J. Fuchs, T. Stiewe, A. Ö. Yildirim, F. Bamberg, *et al.*, Physica Medica **30**, 352 (2014).
[16] K. Scherer, A. Yaroshenko, D. A. Bölükbas, L. B. Gromann, K. Hellbach, F. G. Meinel, M. Braunagel, J. Von Berg, O. Eickelberg, M. F. Reiser, *et al.*, Scientific Reports **7**, 402 (2017).
[17] L. B. Gromann, K. Scherer, A. Yaroshenko, D. A. Bölükbas, K. Hellbach, F. G. Meinel, M. Braunagel, O. Eickelberg, M. F. Reiser, F. Pfeiffer, *et al.*, Medical Imaging 2017: Physics of Medical Imaging **10132**, 101325L (2017).
[18] A. Velroyen, A. Yaroshenko, D. Hahn, A. Fehringer, A. Tapfer, M. Müller, P. Noël, B. Pauwels, A. Sasov, A. Ö. Yildirim, *et al.*, EBioMedicine **2**, 1500 (2015).
[19] V. Revol, C. Kottler, R. Kaufmann, I. Jerjen, T. Lüthi, F. Cardot, P. Niedermann, U. Straumann, U. Sennhauser, and C. Urban, Nuclear Instruments and Methods in Physics Research Section A: Accelerators, Spectrometers, Detectors and Associated Equipment **648**, S302 (2011).
[20] T. Thüring, P. Modregger, T. Grund, J. Kenntner, C. David, and M. Stampanoni, Applied Physics Letters **99**, 041111 (2011).
[21] E. Reznikova, J. Mohr, M. Börner, V. Nazmov, and P.-J. Jakobs, Microsystem Technologies **14**, 1683 (2008).
[22] J. Kenntner, T. Grund, B. Matthis, M. Börner, J. Mohr, T. Scherer, M. Walter, M. Willner, A. Tapfer, M. Bech, *et al.*, Developments in X-Ray Tomography VII **7804**, 780408 (2010).
[23] J. Kenntner, V. Altapova, T. Grund, F. J. Pantenburg, J. Meiser, T. Baumbach, and J. Mohr, AIP Conference Proceedings **1437**, 89 (2012).

[24]J. Mohr, T. Grund, D. Kunka, J. Kenntner, J. Leuthold, J. Meiser, J. Schulz, and M. Walter, AIP Conference Proceedings **1466**, 41 (2012).
[25]T. Rodt, M. Lüpke, C. Böhm, C. von Falck, G. Stamm, J. Borlak, H. Seifert, and M. Galanski, Acta Radiologica **52**, 75 (2011).
[26]A. P. Dempster, N. M. Laird, and D. B. Rubin, Journal of the Royal Statistical Society: Series B (Methodological) **39**, 1 (1977).
[27]C. B. Do and S. Batzoglou, Nature Biotechnology **26**, 897 (2008).
[28]D. Hahn, P. Thibault, A. Fehringer, M. Bech, T. Köhler, F. Pfeiffer, and P. B. Noël, Scientific Reports **5**, 10452 (2015).
[29]J. Bian, J. H. Siewerdsen, X. Han, E. Y. Sidky, J. L. Prince, C. A. Pelizzari, and X. Pan, Physics in Medicine and Biology **55**, 6575 (2010).
[30]A. Kak and M. Slaney, *Principles of computerized tomographic imaging* (IEEE Press, 1988).
[31]F. Natterer, *The Mathematics of Computerized Tomography* (Vieweg+Teubner Verlag, Wiesbaden, 1986).
[32]Y. Kessener, "X-Ray Imaging: How to compare detector quality with Noise Equivalent Dose," http://info.teledynedalsa.com/acton/attachment/14932/f-04ad/1/-/-/-/-/dpi-Whitepaper-CMOS-NED.pdf (2015), [April-2019].